



Quantitative detection of aerial suspension of particles with a full-frame visual camera for atmospheric wind tunnel studies

E. M. Esders, C. Georgi, W. Babel & C. K. Thomas

To cite this article: E. M. Esders, C. Georgi, W. Babel & C. K. Thomas (2022): Quantitative detection of aerial suspension of particles with a full-frame visual camera for atmospheric wind tunnel studies, *Aerosol Science and Technology*, DOI: [10.1080/02786826.2022.2048789](https://doi.org/10.1080/02786826.2022.2048789)

To link to this article: <https://doi.org/10.1080/02786826.2022.2048789>



View supplementary material [↗](#)



Accepted author version posted online: 03 Mar 2022.



Submit your article to this journal [↗](#)



Article views: 11



View related articles [↗](#)



View Crossmark data [↗](#)

Quantitative detection of aerial suspension of particles with a full-frame visual camera for atmospheric wind tunnel studies

E. M. Esders^a, C. Georgi^b, W. Babel^{a,c}, and C. K. Thomas^{a,c}

^aDepartment of Micrometeorology, University of Bayreuth, Bayreuth, Bavaria, Germany

^bEnvironmental Chemistry and Air Research, Technische Universität Berlin, Berlin, Germany

^cBayreuth Center for Ecology and Environmental Research (BAYCEER), University of Bayreuth, Bayreuth, Bavaria, Germany

CONTACT Esders E.M. eike.esders@uni-bayreuth.de Department of Micrometeorology, University of Bayreuth, Universitätsstraße 30, 95447 Bayreuth, Germany.

ABSTRACT

Aerial suspension is an important process to link potential sources of particles to atmospheric transport. For contaminants like radioactive particles, pesticides or spores aerial suspension is especially relevant. We present a method that can visually quantify the suspension potential of particles in an idealized surface atmosphere system. The suspension potential of an airflow was assessed by quantifying fluorescent microplastic particles on a glass plate and exposing them to an incrementally increasing erosive wind force. In this first application of the method, we demonstrate its utility across a range of microplastic particles with regard to shape, size and polymer composition, and to detect two distinct regimes with different suspension rates. It can yield statistically robust estimates for the suspension potential of suspended fractions of up to 2500 particles at a mean areal number density of 2.6 particles per mm^2 . The mean wind speed at 2.7 cm height reached up to 5.2 ms^{-1} with a corresponding friction velocity of 0.51 ms^{-1} .

Introduction

Turbulent flows suspend particles from surfaces. Suspended particles can be inhaled, for example contaminants like, radioactive particles, pesticides and spores (Krauter and Biermann 2007; Weis et al. 2002; Nicholson 1988; Orgill et al. 1976). Thus, examining the suspension potential of particles is relevant to estimate the potential risk for human health. Further, the suspension potential is crucial for studying the transport of particles, like Saharan dust, nutrients or lately microplastics (Zhang 2020; Goudie and Middleton 2006; Griffin 2001; Savoie 1980; Graham 1979).

The development and emergence of plastic products started in the 1950s and revolutionized industrial, medical, agricultural and many other fields through their unique and versatile properties. Since then, the total amount of plastic produced per year has risen above 300 million tons in the last years (Ritchie and Roser 2018). The valued persistent characteristic of plastics though appears to cause an environmental problem as it leads to the occurrence of microplastics (particles with a diameter $< 5\text{mm}$) in remote locations including Antarctica, Arctic, deep sea (Bergmann et al. 2019; Katija et al. 2017) and other seemingly pristine environments (Stefánsson et al. 2021; Brahney et al. 2020; Allen et al. 2019).

These findings suggest that the atmosphere can serve as most important long-range transport pathway to remote areas independent of rivers or water bodies. In spite of the potential large contribution of the atmosphere to the dispersion of solid particles including microplastics, little attention has been devoted to atmospheric transport and interface processes (SAPEA 2019). In contrast, the number of publications assessing microplastics and their behaviour in the hydro- and pedosphere has been increasing for years. Several studies pointed out that the atmospheric limb needs to be examined more deeply for a holistic understanding of global microplastic cycle (Brahney et al. 2021; Can-Güven 2020; Mbachu et al. 2020; Zhang 2020). A variety of sources can emit microplastics into the atmosphere such as incineration of waste, wear of synthetic fibers from clothing, sewage sludges and tire erosion if rubber is included (Environment 2020). The presence of microplastics in total atmospheric fallout was first pointed out by

Dris et al. (2015) in the urban area of Greater Paris. Hereafter more studies on deposition were done such as Allen et al. (2019) who pointed out a potential atmospheric long-range transport of microplastics. Typical fragment and fibre sizes found in deposition studies are smaller than 100 μm in diameter and 900 μm in length, respectively (Allen et al. 2019; Klein und Fischer et al. 2019; Vianello et al. 2019). Due to analytical limitations the smallest microplastics found in air samples were $\geq 2\mu\text{m}$ (Levermore et al. 2020; Prata et al. 2020; Allen et al. 2019; Klein und Fischer et al. 2019; Vianello et al. 2019). Only recently micro and nanoplastics with diameters $\leq 2.5 \mu\text{m}$ were measured, which corresponds to the typical size class that air pollution research focuses on (Rahman et al. 2022). Several studies determined deposition rates of microplastics, but fewer studies have focused on how microplastics are entrained or suspended into the atmosphere. Only studying the whole life cycle will reveal the fate of atmospheric microplastics. The life cycle starts at primary and secondary sources. The transport of microplastics includes processes of suspension, characteristics of short- and long-range transport as well as wet and dry deposition mechanics.

Measuring suspension rates at different erosive wind forces for specific particle surface combinations yields information about the suspension potential. The suspension rate is defined as the number of particles leaving a known surface area per unit time. It can be quantified in different fashions. One approach is to measure the number of particles ex-situ before and after an experiment. Ex-situ measurements have the advantage of high spatial resolution, but information about suspension rates over time is reduced (Rezaei et al. 2019; Kim et al. 2016; Reeks and Hall 2001). Further, disadvantages can emerge by handling the sample or particle aging effects (Kim et al. 2016). An alternate approach is to measure the particles in-situ, either by measuring the number of particles entrained in the air flow (Bullard et al. 2021; Krauter and Biermann 2007; Nicholson 1993), or by counting the number of particles on a test surface by optical means using a camera (Ibrahim et al. 2004; Soltani and Ahmadi 1994; Wu et al. 1992). The later approach allows measuring with much higher time resolution, which may be helpful in providing insights into different modes of suspension. The modes of suspension can be sliding, rolling, bounceoff and entrainment (Soltani and Ahmadi 1994; Wu et al. 1992). A potential disadvantage of in-

situ measurements is that usually a smaller area is observed, and hence a smaller number of particles can be examined simultaneously, which reduces its statistical robustness.

This paper presents an in-situ approach to measure the suspension potential of a variety of particle types using a wind tunnel, a visual full-frame camera and an idealized particle surface combination, namely a glass plate and fluorescing primary microplastics. While the presented method can be applied to a variety of solid particles across a size-range from 50 to 215 μm , developing this optical method was motivated by the emergence of microplastics. The goal of this paper is to evaluate the method we developed by discussing the precision of the achieved measurements.

Finally, we propose the following research questions:

- Does the proposed method yield meaningful estimates for the suspension potential of microplastics?
- Can the approach be used on a variety of microplastics?

2. Methods

2.1. Wind tunnel

The wind tunnel in which the experiments were conducted had a total length of 730 cm with a cross section of 60 cm x 120 cm in width and height, respectively (see Fig. 1). At the inflow section, a honeycomb structure ensured laminar flow conditions. The air passed through the contraction zone and before leaving the wind tunnel it was filtered by a HEPA filter (EU2, 10 μm pore size, Erwin Telle GmbH, Germany). The airflow speed in the wind tunnel was adjusted using a set of twelve fans of diameter 26.5 cm (RAB O TURBO 250, DALAP GmbH, Germany) whose rotation speed was controlled using a transformer (LSS 720-K, Thalheimer Transformatoren GmbH, Germany).

“Figure 1”

In the contraction zone of the wind tunnel the cross section narrowed to 27 cm width and 54 cm height. All inner walls in the contraction zone were lined with extruded polystyrene foam. A potential

contamination of the test section with polystyrene particles from the inner walls was irrelevant for our setup, as only fluorescent particles were captured in the analysis while the wall lining was not fluorescent. The contraction zone was accessed through two hatches. At the start of the contraction zone, turbulence was shear-generated by a carefully chosen set of cones (see Tab. S1). In addition, roughness elements were placed on the bottom of the wind tunnel reaching from the cones all the way to the test section. The test section was prepared to measure the suspension of fluorescent microplastic particles (fMPPs) from a 76 x 26 mm glass plate (microscope slides, Thermo Scientific). The glass plate was mounted in the test section such that its surface was at the same level as the top of the roughness elements. Above the glass plate a constant temperature anemometer (CTA) was installed (three-dimensional wire probe, Model 55P095, Dantec Dynamics, controller, Model 54T42, Dantec Dynamics) to measure the flow statistics. At the end of the contraction zone a temperature and relative humidity sensor was installed (Model HC2A, rotronic). Further, the temperature probe of the CTA (Model 90P10, Dantec Dynamics) was installed there. A camera was placed beneath the test section and focused on the glass plate installed in the test section. A window in the bottom of the test section enabled the camera to focus on the glass plate. The relative humidity was about 20 % during all experiments.

2.2. Turbulence measurements

The turbulent flow field was measured with a CTA at a frequency of 10 kHz. The CTA was calibrated with a two-point calibrator (Model 55H02, Dantec Dynamics) before the first measurement each day. It was mounted on a 1D-traverse (Lightweight Traverse, ISEL) that automatically moved the CTA into the desired z-position in the wind tunnel. Wind profiles were measured at seven specific heights assuming a logarithmic wind profile forming at the lower contraction zone boundary reaching from $z = 6$ mm to $z = 27$ mm (see section *Wind tunnel characteristics* 3.1 for why this range was chosen). The wind profiles were measured to verify the existence of a well-developed logarithmic wall boundary layer, which resembles outdoor conditions. Data from the CTA were collected for 30 s at every point of the profile and the obtained turbulence raw data was automatically temperature-corrected by the CTA software (Streamware Basic v6.10, Dantec Dynamics) using the temperature measurement of the 90P10. Turbulent

fluxes including the friction velocity and other flow statistics were computed using the software tool 'bmmflux' of the Micrometeorology Group of the University of Bayreuth (see Appendix in Thomas et al. 2009) and 3D-rotated to eliminate the mean vertical and crosswind wind speed components. The velocity components of the main wind, cross wind and vertical wind were defined as u , v and w , respectively. For comparison purposes the friction velocity u_* was determined in two fashions. First, it was derived from the logarithmic wind profile measured in the wind tunnel assuming the functional form of:

$$u_{*,Pr} = \kappa \cdot \frac{\partial \bar{U}}{\partial \ln(z)} \quad (1)$$

Hereafter referred to as $u_{*,Pr}$, and secondly calculated as the arithmetic mean of the directly measured density-normalized momentum flux u_* using the EC approach in the height profiles:

$$u_{*,EC} = \frac{1}{n} \sum_{i=1}^n \sqrt{-u'w'} \quad (2)$$

which yields $u_{*,EC}$ for every height measured of the wind profile.

2.3. Fluorescent microplastic particles

Three different types of fluorescent microplastic particles (fMPPs) were analyzed to develop and verify the detection and quantification method regarding size range, shape and fluorophores. Type A and B were spherical monodispers fMPPs made of polyethylene (PE) with a diameter range of 53 to 63 μm and 215 to 250 μm , respectively (both manufactured by Cospheric, Santa Barbara, United States of America). fMPP type A contained a green fluorophore and fMPP type B contained a red fluorophore. Type C were polydispers irregularly shaped fMPPs made of polystyrene (PS). The size was defined with the maximum size fitting through a 125 μm mesh and the minimum size not fitting through a 75 μm mesh. Type C contained Rhodamin B as fluorophore and was produced at the Macromolecular Chemistry department, University of Bayreuth.

2.4. Camera setup

A full-frame visual camera (Model Alpha 7R II, Sony) equipped with a macro lens (Model SEL90M28G, Sony) took images of the fMPPs placed on the glass plate in the test section. The camera was installed directly beneath the test section (see Fig. 1) facing upward through a window in the base of the wind tunnel and was focused on the fMPPs placed on the glass plate. The camera was mounted on a small manual lift used to manually focus the camera on the fMPPs to maintain the camera's magnification ratio constant at 1:1. At this magnification ratio the distance in an image precisely corresponds to that in nature. The camera was set to an ISO of 51200, an aperture of 2.8 and a shutter speed of 1/320 sec for fMPPs type A and B. For fMPPs type C the ISO was set to 10000, an aperture of 2.8 and shutter speed of 1/10 sec. Images were taken in raw-format and the resolution was set to 42 MP (5304x7952). The camera was controlled from a computer via tethering using the software package Capture One 20 (Phase One, Frederiksberg, Denmark). Two commercially available ultra-violet lights (45 cm, 15 W, EUROLITE) were placed next to the camera, to excite the fMPPs placed on the glass plate. In this setup the field of view was 861,6 mm². Other camera sensor formats could be used for the method. At a magnification ratio of 1:1 the camera sensor area directly corresponds to the field of view. Thus, a smaller camera sensor would yield a smaller field of view limiting the number of particles to be detected while keeping the same particle seeding density.

2.5. Particle detection

We developed a software tool hereafter referred to as 'mp.flux' for particle detection using the images taken with the visual full-frame camera. The code is written in the software environment 'julia' (Bezanson et al. 2017) and is available on zenodo (Esders et al. 2021). MP.flux can count the total number of fMPPs residing on the glass plate (N), it can calculate the number of pixels a detected particle contains (N_p) and the suspension rate of fMPPs ($\frac{\Delta N}{\Delta t}$) using a series of images.

2.5.1. Suspended fMPP fractions

The fraction of fMPPs that was suspended at a specific experimental stage relative to the start value of N , was defined as:

$$N_k^* = \frac{N_{(k)} - N_{(k-1)}}{N_{(t0)}} \quad (3)$$

where $N_{(k)}$ is N at the end of the suspension stage, $N_{(k-1)}$ is N at the beginning of the suspension stage, and $N_{(t0)}$ is the mean initial value of N determined from the first ten images at the start of the experiment.

2.5.2. Description of the detection algorithm

Here we briefly describe the general steps the algorithm performed to distinguish fMPPs from the background. The camera software saved the image data in a RAW format, which were subsequently manually converted into TIF format using the software tool Capture One 20 (Phase One, Frederiksberg, Denmark). The TIF image was loaded as a three-dimensional RGB array into the workspace of the software environment. Values in the horizontal and vertical axis of the array are referred to as x-axis and y-axis, respectively. Values in this plane represent the intensity of a RGB color measured by the pixels of the camera sensor. The depth or z-axis of the array represented the different RGB channels. For further processing, the array was subset to only the RGB channel that corresponded to the fluorophore color of the fMPP type used in the experiment (green for fMPP type A, red for fMPP type B and fMPP type C). The array was filtered by a color intensity threshold (CIT), setting color values smaller than the CIT to zero and setting color values equal to or greater than the CIT to one. In a next step proceeding column-wise spatially connected clusters of pixels with a value of one were identified and saved separately, and then checked if the clusters were connected horizontally between neighboring columns. A connection was recognized if two clusters contained at least one pair of pixels that had the same y-value and a difference of one in their x-values. If they were connected, clusters were combined to a particle. This process was iterated until no further connections were found. Finally, only particles containing a minimum number of pixels (N_f) were included for calculating N .

2.5.3. Color intensity threshold

As described above the image data was filtered with a color intensity threshold (*CIT*). The *CIT* is applied to separate the fMPPs from the background. We chose the following approach to identify the optimal *CIT*. One image in a series for each experiment was selected for the analysis. The image was cropped to a size which contained a few fMPPs which could easily be visually counted (see Fig. 2). Then, the software determined N with *CITs* ranging from 0.02 to 0.98 in 0.02 steps.

“Figure 2”

This procedure will find ranges of *CITs* that determine the same N (see Fig. 3). The final *CIT* was determined as the midpoint of the *CIT* range, that determined N equal to the visually counted N . The chosen range should at least cover an extent of 0.1 *CITs*. If multiple ranges are found that satisfy this criterium, we recommend choosing the wider range. The defined *CIT* was then used for the whole series of images of an experiment.

“Figure 3”

2.5.4. Determination of N_f for fMPP type A and B

Particles were filtered according to a minimum number of pixels (N_f). The filter value N_f was determined with a normal distribution fitted to the main peak found in the histogram of N_p . The value N_f was defined as:

$$N_f = \mu - 2.576\sigma \quad (4)$$

where μ is the mean of the normal distribution and σ its standard deviation.

2.5.5. Determination of N_f for fMPP type C

Due to its polydisperse nature, the N_p histogram for fMPP type C did not contain one main peak. Thus, fitting a normal distribution to the data to identify the filter value N_f presented challenges. Therefore, the distribution parameters for fMPP type C were derived from the original size distribution of the particles provided in the data sheet (see Fig. S10). Hereafter the conversion from the mean diameter found in the

data sheet to number of pixels per particle is described. The number of pixels per particle (N_p) was assumed as the area of a particle (A_{par}) divided by the area of a single pixel (A_{pix}).

$$N_p = A_{par}/A_{pix} \quad (5)$$

The area of a particle (A_{par}) was computed as:

$$A_{par} = \pi \left(\frac{D_{par}}{2}\right)^2 \quad (6)$$

where A_{par} is the area of a particle in μm^2 and D_{par} is the diameter of a particle in μm . Here the mean diameter found in the data sheet was inserted for D_{par} . The variable A_{pix} was calculated as follows:

$$A_{pix} = \frac{W}{7952} \frac{H}{5304} \quad (7)$$

where A_{pix} is the area of a pixel in μm^2 , W is the width of the camera sensor in μm , H is the height of the camera sensor in μm , 7952 is the number of pixels in width and 5304 is the number of pixels in height. Now A_{par} divided by A_{pix} gives the mean number of pixels per particle for fMPP type C. The same way using the standard deviation from the data sheet instead of the mean, the standard deviation of the number of pixels per particle was calculated. As mentioned above the magnification ratio was kept at 1:1. Thus, the area represented by a pixel was constant and therefore the relation of the diameter of a particle to the number of pixels it contained was also constant.

2.5.6. Error analysis

Here we describe how the precision of estimating N and \bar{N}_p was examined including the impact of vibrations from the fans of the wind tunnel, which started to affect images at wind speeds exceeding 3.1 ms^{-1} . The vibrations moved the glass plate and therefore led to image blurring. The following method was employed to quantify the relative standard deviation of estimating N and \bar{N}_p from the blurred imagery with the true values being held constant. A glass plate with fMPPs type A was prepared and placed in the

test section. It was completely shielded from the wind, thus only the vibration would affect the fMPPs and N could be assumed to be constant. Three sets of thirty images were taken with two different camera setups and at two different wind speeds. The first set of images used the camera settings (A) ISO 2500, an aperture of F 2.8 and a shutter speed of 1/10 s. The wind tunnel remained switched off ($\bar{U}_{27mm} = 0 \text{ ms}^{-1}$). This set represents suitable camera settings without vibrations and was used as a reference. The second set of images used identical camera settings (A), but \bar{U}_{27mm} was raised to 5.2 ms^{-1} . The third set of images used the camera settings (B) of ISO 51200 and a shutter speed of 1/320 s at a wind speed of $\bar{U}_{27mm} = 5.2 \text{ ms}^{-1}$.

The estimated total number of particles (N) was smaller for set two and three compared to the first (see Tab. 1). The mean number of pixels a particle contains (\bar{N}_p) was smaller estimated for set three and higher estimated for set two compared to set one. The relative standard deviation of N and \bar{N}_p were highest for set two followed by set three and lowest for set one.

“Table 1”

In the suspension experiments camera setup B was used for fMPP type A and B. For fMPP type C different settings were employed, as with a shutter speed of 1/320s the contrast between the fMPPs and the background was too small to detect them. The ISO was set to 10000, the aperture to F 2.8 and the shutter speed to 1/10 s.

2.6. Suspension experiments

Here the procedure of conducting a suspension experiment is described. First a glass plate was inoculated with one type of fMPPs. The fMPPs type A and C were brought onto the glass plate via the sealing cap of their containers. The closed fMPP container was flipped once, thus a small amount of fMPPs would adhere to the sealing cap. Then the sealing cap was screwed off the container and by tipping on the top of it while holding it above the glass plate small amounts of fMPPs could be released onto the glass plate. The fMPPs of type B could be placed on the glass plate directly from their container by tipping on the

container while holding it slightly angled facing to the glass plate. The number of fMPPs brought onto the test surface could be visually approximated or checked via the camera. Particles were applied until at least 200 particles were on the glass plate in the field of view of the camera. This number was targeted to ensure that also the particle surface connections with a small probability (very weak and very strong binding forces) would have statistically robust sample sizes. Despite the manual inoculation, fMPP densities were consistent in a test series of 18 inoculations: of all square millimeters containing at least one particle, 87 % contained ten or less particles and 34 % contained three or less particles (see Fig. S9). After the glass plate was inoculated with fMPPs, it was placed in the test section and the wind tunnel was closed. The UV lights were turned on and the light in the lab was turned off so that the camera would only detect light emitted by the excited fMPPs. The camera was started to take photos every ten seconds. For the first ten images of suspension stage zero the relative standard deviation (c_v) was calculated. In suspension stage zero the air speed was zero and N was assumed to be constant. Thus, the variation in N represents the noise by the measurement without vibrations. Then the airflow speed was set to the suspension stage one. After 6 minutes (fMPP type A and C) or 8 minutes (fMPP type B) the next suspension stage was employed. This process was repeated until the last suspension stage finished, or all fMPPs were suspended. All particles were suspended only for fMPP type B.

2.7. Resolving the suspension potential

Here we describe the method of how to quantify the suspension potential of fMPPs. Several studies showed that individual particles of a particle population are suspended from a surface at different frictional eroding forces (Ibrahim et al. 2004; Wu et al. 1992). This finding can be explained by recalling that every particle is bound by adhesion forces specific for each particle. The distribution of these adhesion forces follows a log-normal law (Zimon 1982). Hence, for a given frictional eroding force exerted onto a particle population, only the fraction of particles bound by adhesion forces smaller or equal to the acting frictional eroding force are suspended. In the proposed method the erosive wind force is raised incrementally during an experiment by adjusting the airflow speed to resolve these fractions bound by different adhesion forces. This process allows linking a suspended fraction of particles to the acting

erosive wind force. The friction velocity ($u_{*,EC}$) was employed as the proxy for the frictional eroding forces as it represents the density-normalized momentum flux. Each suspension experiment contained six specific suspension stages. The first stage started with $u_{*,EC} = 0$ and for every following suspension stage $u_{*,EC}$ was increased, ranging from $u_{*,EC} = 0 \text{ ms}^{-1}$ to $u_{*,EC} = 0.51 \text{ ms}^{-1}$. For fMPPs which suspended at a specific stage the current $u_{*,EC}$ was defined as their threshold friction velocity ($u_{*,th}$).

3. Results

3.1. Wind tunnel characteristics

The measured vertical profiles showed a logarithmic wind profile and a height-constant standard deviation of the mean horizontal wind speed (see Fig. S1, S2). The mean horizontal wind speed at the top of the profile \bar{U}_{27mm} ($z = 27 \text{ mm}$, aerodynamic height) ranged from 0.9 to 5.2 ms^{-1} . The friction velocity (u_*) computed from the two different methods introduced in section 2.2 can be expressed as:

$$u_{*,Pr}(\bar{U}_{27mm}) = 0.094 \cdot \bar{U}_{27mm}; R = 0.99 \quad (8)$$

$$u_{*,EC}(\bar{U}_{27mm}) = 0.103 \cdot \bar{U}_{27mm}; R = 0.99 \quad (9)$$

The $u_{*,Pr}$ was about 10 to 15 % percent higher than the $u_{*,EC}$ for $\bar{U}_{27mm} > 3.1 \text{ ms}^{-1}$ (see Tab. 2). For values $\bar{U}_{27mm} < 3.1 \text{ ms}^{-1}$ both approaches yielded the same values for u_* within 10% error bounds. The roughness length (z_0) was calculated by extrapolating the logarithmic wind profile:

$$\bar{U}(z) = \frac{u_*}{\kappa} \ln\left(\frac{z}{z_0}\right) \quad (10)$$

to the height z where $\bar{U} = 0$, giving $z_0 = 0.4 \text{ mm} \pm 0.1$.

“Table 2”

The turbulence power spectra of the velocity components $\overline{u'u'}$, $\overline{v'v'}$ and $\overline{w'w'}$ showed the following characteristics: the peak frequency of the horizontal components $\overline{u'u'}$ and $\overline{v'v'}$ was shifted toward lower frequencies compared to the that of the vertical component $\overline{w'w'}$ (see Fig. S4). All three normalized power spectra decrease in the inertial subrange with a slope close to the expected $-2/3$ decay. The normalized power in the inertial subrange of the $\overline{u'w'}$ co-spectrum decreases with an expected slope close to $-4/3$. The frequency spectra suggest that turbulence has fully developed in the wind tunnel.

The wind profile was determined at seven different heights ranging from $z = 6$ mm to $z = 27$ mm to calculate the boundary layer characteristics. Above $z = 27$ mm an internal boundary layer formed which did not represent the local surface characteristics at the test section (see Fig. S3). Thus, measurements above 27 mm seem to be outside of the equilibrium layer formed by the roughness elements placed in the test section. The wind profile showed consistent u_* between adjacent measurement heights within 1 to 5 % and therefore represents a uniform wall boundary layer. One recalls that u_* determined across this height range is a measure of the frictional eroding forces exerted onto the glass plate leading to particle suspension (Ibrahim et al. 2004; Loosmore 2003). The wind profile measurements showed small variations in $\frac{\partial \bar{U}}{\partial \ln(z)}$ across the individual wind speeds (see Fig. S2). Using a 95 % confidence interval of the linear model describing the relation of u_* to $\frac{\partial \bar{U}}{\partial \ln(z)}$ the estimate for u_* varies about 10 % at $\bar{U}_{27mm} = 0.9 \text{ ms}^{-1}$ and decreases to about 3 % variation at $\bar{U}_{27mm} = 5.2 \text{ ms}^{-1}$. Thus, the variation in u_* resulting from the measurement and computational uncertainty is much smaller than the difference between u_* values employed across the suspension stages and is therefore negligible for the analysis of the particle suspension potential.

3.2. Color intensity threshold

Here the results of the evaluation of the color intensity threshold (*CIT*) are presented and explained. As described above we chose the *CIT* by comparing a visually determined N with the determined N over the full range of *CITs*. In the range of *CITs* from 0.25 to 0.45, N is determined equal to the visually

determined N (see Fig.3). Thus, the midpoint of this range, 0.35, was employed for the processing of the images of fMPP type A (see Fig. S5 for the CIT evaluation of fMPP type B and C).

Further, the estimate for N dramatically varies for CIT s from zero to one. At CIT s below 0.12 the estimates for N goes up to 748. At such low CIT s the background noise of the camera sensor is not filtered. Hence large quantities of non-existent very small particles are being detected and N is greatly overestimated (see Fig. S13). In the CIT range from 0.11 to 0.49 the estimate for N is the same for four ranges and increases stepwise from 23 to 27. The estimate for N is more consistent in this range, as the contours of particles are well defined, and the camera sensor noise is filtered (see Fig. S20). A detailed analysis of clusters formed by single particles explains why the estimate increases stepwise (see Fig.4). Pixels that touch vertically or horizontally are detected as a single particle. The individual pixels are colored corresponding to the color bar at the right-hand side of Figure 4, with dark to bright colors representing low to high color intensities.

“Figure 4”

Hence, if a CIT of 0.15 would be applied, all pixels in the darkest color would be filtered. As seen in Figure 4 individual clusters can be separated at different CIT values, as with higher CIT s the pixels connecting the particles are eventually filtered and the particles are detected separately. Thus, in the CIT range from 0.12 to 0.49 more and more particles are detected as singlets and not as a cluster. Note that by visually counting N a decision must be made, which particles should be counted as singlets. We recommend choosing the CIT range that separates particles where a decrease in c_i between the particles is clearly visible. Further, at small areal number densities (particles per unit area) the number of clusters that cannot be separated by the CIT is very small, hence the estimate for N is reasonable.

For CIT values above 0.49, the estimate for N again varies dramatically. Here particles consisting only pixels with low color intensities vanish and at CIT s greater than 0.67 the residing particles are fragmented into their brightest single pixels (brightest color in Fig.4).

3.3. N_p histogram

The N_p histogram for fMPP type A and fMPP type B is unimodal and bell-shaped (see Fig. 5). There are also smaller peaks outside of the distribution at smaller and greater N_p values. The N_p values in the N_p histogram for fMPP type C are randomly distributed and the histogram is multimodal.

“Figure 5”

Particles were filtered by the number of pixels they contain (N_p). Thus, only particles with a minimum number of pixels (N_f) were considered for the estimation of N . We chose to employ a filter, as in the single digit range of N_p values the number of particles varied strongly from image to image, which increased the variability of N . The proposed method to determine N_f is based on the normal distribution of the diameters of the individual fMPP types. Particles much smaller than the majority of particles should be excluded, as they do not represent the particles targeted for the suspension potential. This step reduced the variability in N . Mean and standard deviation for the fitted distributions in Figure 5 are as follows: type A 152 ± 24 , type B 2400 ± 170 and type C 641 ± 79 in the unit of pixels per particle.

3.3.1. N_p histogram: Irregular shaped particles

For fMPP type C no main peak was found (see Fig. 5), likely due to their irregular shape and polydispersity. In the fashion the images were taken in this method a spherical particle always represents the same area despite its orientation if located plainly on the surface, but for irregular particles the area might be different depending on the orientation of the particle. Moreover, for fMPP type C the shutter speed could not be run at 1/320s and was run at 1/10s instead. Thus, blurring of the particles by vibrations were present leading to an increased N_p . This also led to a widening of the range of N_p , as the strength of the blurring varies from image to image additionally leading to an increase in N_p . If no main peak in the histogram to determine N_f is found, the particles' size distribution can be used as an alternative instead.

3.4. Suspension experiments

Now we present the results that proof the method's functionality. Suspension of particles was observed with high precision for all three fMPP types and the suspension stages are clearly visible (see Fig. 6). For fMPP type A, B and C the relative standard deviation (c_v) in suspension stage zero was 0.2 %, 0.2 % and 0.5 %, respectively.

“Figure 6”

At the start of a new suspension stage the suspension rate ($\frac{\Delta N}{\Delta t}$) was largest leading to a fast decreasing N . Then the suspension rate decreased until no additional particles were suspended from the glass plate. Detecting two distinct suspension regimes, namely a high suspension rate followed by a low suspension rate, is characteristic of suspension and further evidence of the applicability of the method (Ibrahim et al. 2004; Wu et al. 1992; Jurcik and Wang 1991; Wen and Kasper 1989). The dynamics of $\frac{\Delta N}{\Delta t}$ are discussed in more detail in the section 4.4.

The suspended fractions N^* with respect to the threshold friction velocities can be interpreted as the suspension potential of the respective fMPP type (see Fig. 7).

“Figure 7”

From fMPP type B to A to C the suspension potential decreases, meaning fMPP type B is suspended at low eroding forces and C at high eroding forces. Note that for B and C not all particles were suspended and thus the suspension potential is not resolved for higher friction velocities. In general, the suspended fractions N^* per suspension stage were different for all three fMPP types and indicate the different suspension potential of the respective fMPPs (see Tab. 2). For some suspension stages sudden decreases in N were found (see Fig. 6; fMPP type A suspension stage two; fMPP type B suspension stage two). These might be the effect of collisions of single fMPPs, that while detaching from the glass plate collide with other fMPPs and causing them to be suspended, which in turn led to a sudden decrease in N .

Now the differences in the suspension potential are discussed. For fMPP type A and C, no significant amounts of fMPPs were suspended in the first two and four suspension stages, respectively. In all other

suspension stages fMPPs were suspended. For fMPPs type B, all particles were suspended completely at the end of suspension stage four. The fMPPs type B are spherical and have the largest diameter. Therefore, they are expected to be suspended at smaller u_* than fMPP type A and C, as their effective surface area (πr^2) exposed to the momentum force of the wind is larger (Soltani and Ahmadi 1994). For fMPPs type A a larger fraction of particles was suspended at the end of the suspension experiment than for fMPPs type C. Here fMPPs type C are the larger particles, hence the size does not explain the difference in this case. The irregular form of fMPP type C probably led to the different suspension potential. The effect of an irregular form can either increase or decrease the binding force to the surface (Zimon 1982). In our case, the binding force must have been increased, as all other parameters were held constant compared to the other particle suspension experiments. In general, many factors influence the suspension potential, for example relative humidity, deposition technique, residence time, air flow acceleration (Kim et al. 2016; Ibrahim et al. 2004; Wang 1991). Studying these effects was out of the scope of this paper.

3.5. Time constant

Suspension rates are a relevant measure to compare individual suspension stages. The time constant (τ) is used in this paper to compare the suspension rates of individual suspension stages. The time constant is a time scale that corresponds to the time it takes a signal starting at a value of one to decrease to a value of $\frac{1}{e}$. It is independent of the step change, i.e., number of particles suspended. A small τ in relation to the length of time of the whole suspension stage implies higher suspension rates at the beginning of a suspension stage. In suspension stages where $N^* > 0$, the decrease in N could be described with an exponential decay function of the following form:

$$N(t) = N_{(t2)} + (N_{(t1)} - N_{(t2)}) * e^{-\frac{t}{\tau}} \quad (11)$$

where $N(t)$ is N at time t , $N_{(t1)}$ is N at the beginning of the suspension stage, $N_{(t2)}$ is N at the end of the suspension stage, t is the time in seconds and τ is the time constant. In most cases the time constant varied

between 70 and 195 seconds (see Tab. 2). For fMPP type A and B the time constant seemed to be smaller for suspension stages with high N^* . In almost all stages the suspension rate decreased close to zero at the end of a suspension stage except for suspension stage one of fMPP type A and suspension stage six of fMPP type C (see Fig. 8).

“Figure 8”

4. Discussion

4.1. Choosing suitable camera settings

Vibrations from the fans blurred the images at wind speeds around 3.1 ms^{-1} . The blurring had two effects on the particle detection. First, blurred particles had increased numbers of pixels per particle (N_p). Second, particles close to each other were merged to one single big fMPP, decreasing the estimate of fMPPs residing on the glass plate (N). Occasionally the images in set two (camera setup A and vibrations) were sharp and N was close to N determined in set three (camera setup B and vibrations, see Fig. S8). The occasional sharp images are probably the result of a change in the displacement speed of the glass plate by the vibrations. Hence in cases where the displacement speed was low even the slower shutter speed was sufficient to acquire sharp imagery of the particles. The fast shutter speed ($1/320 \text{ s}$) in set three constantly helped obtaining sharp images and therefore compensated the fluctuations of the estimate for N and N_p , which resulted in the lower relative standard deviation (c_v). Compared to set one, which represented suitable settings (camera setup A and no vibrations), N was slightly underestimated by 17 particles. The lower estimate for N is the result of 17 fMPPs, that merged with another fMPP to a single big fMPP, due to the lowered image quality (vibrations, faster shutter speed and high ISO settings) compared to set one. The relative difference of the estimate of N between set one and three is 1%, thus camera setting B is also a suitable camera setting.

The vibration blurred the fMPPs up to 6 six pixels in the horizontal plane (see Fig. S6). Thus, the blurring effects small fMPPs stronger than bigger fMPPs. Typical diameters for fMPP type A, B and C were 15, 55 and 35 pixels, respectively.

A fast shutter speed reduced the blurring by vibrations, but also came with a drawback. The faster the shutter speed the smaller is the amount of light available for the camera sensor resulting in poorer defined particle contours (see Fig. S6). For fMPP type A and B the ISO had to be set to 51200, to take an image where the fMPPs were bright enough to be distinguishable from the background. The higher sensitivity of the sensor introduces more variation in the pixels color intensity (c_i) contained by a particle (Data not shown). Usually, the brightest pixels are in the center of a detected particle, but with the higher variation in c_i it is more likely that a bright particle is outside of the center of the particle. Thus, a bright pixel can be detected separately from its original fMPP as the CIT filters the pixels with a lower c_i surrounding the bright pixel (see Fig. S7). These particles typically contained less than ten pixels and could be effectively filtered by the N_p filter. Thus, this artefact had no impact on the precision of estimating N .

For fMPP type A and B, it was possible to measure with a fast shutter speed (1/320 s). For fMPP type C a slow shutter speed was used (1/10 s) as the emitted light was too weak to use the same shutter speed. The noise due to the slower shutter speed is relatively small for fMPP type C compared to the effect shown in the vibrations experiment. Probably, for fMPP type C the smaller initial number of particles $N_{(t0)}$, the resulting lower areal number density and the greater N_p reduced the effect of blurring on the underestimation of N and increase in c_v .

4.2. Resolving the suspension potential

The precision of u_* is important, to yield a robust link between the employed u_* and the resulting suspended fraction N^* . In our first approach to demonstrate the method we used the same u_* values for all three fMPP types to show the different suspension behaviour at the same erosive wind forces. In suspension stage two of fMPP type B 70 % of the particles suspended. The suspension potential in this range could have been resolved with more detail by employing smaller steps in u_* . As mentioned above we aimed for at least 200 particles on the glass plate in the field of view of the camera. We suggest a suspension stage to yield a N^* of at least 10 % to obtain a sample size of $N = 20$ per suspension stage. Further, at most 20 % of the initial number of particles should be suspended per suspension stage to

obtain at least five suspension stages. Five values of N^* should suffice to interpolate the relation of N^* to $u_{*,th}$. The suspension potential could only be fully resolved for fMPP type B. For fMPP type A and C higher u_* would be needed to resolve the suspension potential completely.

A large fraction of type B fMPPs got suspended in suspension stage two. As the areal number density was still high, the chance of a fMPP colliding with another fMPP while leaving the glass plate was high. Particle-particle collisions are effective in suspending particles from the surface (Ibrahim et al. 2004). Collisions suspend particles which otherwise would have not been suspended by the given erosive wind forces. Thus, in a suspension stage where a big fraction of N was suspended, N^* is likely to be overestimated and N_u becomes right-skewed. The overestimation of N^* for a suspension stage can be mitigated, by placing the fMPPs on the glass plate with a smaller area number density (Ibrahim et al. 2004). We add, there is an upper limit for particle densities at which too many particles probably overlap and the estimate for the total number of particles on the glass plate would strongly diverge from the real total number of particles. In the most extreme case, all particles would be detected as a single particle. Still at this point the particles could be divided by implementing a watershed segmentation algorithm. Nevertheless, at such densities particle collisions would strongly impact suspension behavior.

4.3. Interpretation of the suspension experiments: distinguishing suspension regimes

Several studies found that during a suspension phase, two regimes with different suspension rates can occur (Ibrahim et al. 2004; Wu et al. 1992; Jurcik and Wang 1991; Wen and Kasper 1989). In the first regime the suspension rate is higher than in the second regime. Ibrahim et al. (2004) argued that the increase of \bar{U} at a given height explains these distinct regimes. In the first regime as \bar{U} increases at the start of a suspension stage also u_* increases and thus in this instationary adjustment period the number of particles, whose $u_{*,th}$ is reached, increases over time. In the second regime \bar{U} and u_* are constant. Here only random stronger eddies, due to the stochastic nature of turbulence, have sufficient erosive force to detach additional particles. We fitted an exponential decay function to N in the individual suspension phases. The time constant (τ) yielded an estimate of how distinct these two regimes are. If τ is small

compared to the length of the suspension stage the two regimes are distinctly different from each other (see Fig. 8). If τ is greater the two regimes are less distinct. According to the idea of Ibrahim et al. (2004) the transition from the first to the second regime should be equal to the time it takes \bar{U} to become constant. For our experiments, a constant wind speed was reached after approximately 10 seconds. This time period is much shorter compared to our determined transition time between regimes. Thus, our findings support the interpretation of Wen and Kasper (1989) that the suspension rate decreases as the number of potentially detachable particles decreases. While one needs to keep in mind that the total number of experiments was relatively small, which potentially opens the door for over-interpreting the results, as this study focuses on developing and verifying the optical detection method, we argue that the time resolution of N is high enough to resolve and examine these two regimes. We add that turbulent airflows are always instationary and random by definition due to their stochastic nature, so if our method can detect both regimes and especially the latter, then it can reproduce physically meaningful results in real-world flows.

5. Conclusion

We present a quantitative detection method that is well suited to measure the suspension potential of particles with differences in size, shape, and polymer. As a proof of principle, the method was demonstrated with three different particle types. The mean wind speed at 2.7 cm height reached up to 5.2 ms^{-1} with a corresponding friction velocity of 0.51 ms^{-1} . The number of particles residing on the glass plate could be estimated with a relative standard deviation of less than 0.5%. For irregularly shaped particles, the size distribution must be known a priori to determine the size filter. The total number of fMPPs on a glass plate (N) was detected by imagery acquired at a shooting frequency of 0.1 Hz, which was fast enough to examine the two distinct regimes that are commonly observed in suspension phases. The in-situ approach allows to use different flow conditions on the same particle population and examine the suspension behaviour in real time. The number of particles that can be examined in a suspension experiment yield statistically robust results. The presented method is a

straightforward approach to study different combinations of particles and surfaces. Requirements for the particles and surfaces are particle diameters equal to or bigger than 50 μm , fluorescent particles, inoculation of particles in a monolayer for accurate estimates, and a translucent test surface. Issues that are addressed in the future are to eliminate the influence of vibrations, taking images from inside the wind tunnel, sampling smaller particles and increase the number of employed suspension stages. Future experiments will use a broader set of surfaces including stainless steel, soil crusts, asphalt, and a larger variety of particles to measure the suspension potential in less idealized systems. The proposed method is a first step toward studying the process of particle suspension in the more complex real world.

Acknowledgments

We like to thank the reviewer and editor for their constructive comments. Further we like to thank Johann Schneider and Johannes Olesch for their technical assistance in constructing and maintaining the wind tunnel laboratory.

Funding

Funded by the Deutsche Forschungsgemeinschaft (DFG, German Research Foundation) – Project Number 391977956 – SFB 1357

References

- Allen, S., D. Allen, V.R. Phoenix, G.L. Roux, P.D. Jiménez, A. Simonneau, S. Binet, and D. Galop 2019. Atmospheric transport and deposition of microplastics in a remote mountain catchment. *Nat Geosci* 12 (5):339–344. doi:10.1038/s41561-019-0335-5.
- Bergmann, M., S. Mützel, S. Primpke, M.B. Tekman, J. Trachsel, and G. Gerdts 2019. White and wonderful? Microplastics prevail in snow from the Alps to the Arctic. *Sci. Adv.* 5 (8):eaax1157. doi:10.1126/sciadv.aax1157.
- Bezanson, J., A. Edelman, S. Karpinski, and V.B. Shah 2017. Julia: A Fresh Approach to Numerical Computing. *SIAM Rev* 59 (1):65–98. doi:10.1137/141000671.
- Brahney, J., M. Hallerud, E. Heim, M. Hahnenberger, and S. Sukumaran 2020. Plastic rain in protected areas of the United States. *Science* 368 (6496):1257–1260. doi:10.1126/science.aaz5819.
- Brahney, J., N. Mahowald, M. Prank, G. Cornwell, Z. Klimont, H. Matsui, and K.A. Prather 2021. Constraining the atmospheric limb of the plastic cycle. *PNAS* 118 (16). doi:10.1073/pnas.2020719118.

- Bullard, J.E., A. Ockelford, P. O'Brien, and C. McKenna Neuman 2021. Preferential transport of microplastics by wind. *Atmos. Environ.* 245:118038. doi:10.1016/j.atmosenv.2020.118038.
- Can-Güven, E. 2020. Microplastics as emerging atmospheric pollutants: a review and bibliometric analysis. *Air Qual Atmos Health*. doi:10.1007/s11869-020-00926-3.
- Dris, R., J. Gasperi, V. Rocher, M. Saad, N. Renault, B. Tassin, R. Dris, J. Gasperi, V. Rocher, M. Saad, N. Renault, and B. Tassin 2015. Microplastic contamination in an urban area: a case study in Greater Paris. *Env. Chem* 12 (5):592–599. doi:10.1071/EN14167.
- Esders, E. M., and Thomas, C. K. 2021, July 13. Particle detection software "mp.flux" used for the publication "Quantitative detection of microplastics with a full-frame visual camera for atmospheric wind tunnel studies" (Version 0.8). Zenodo. <http://doi.org/10.5281/zenodo.5094798>
- Environment, U.N. 2020. Marine Plastic Debris and Microplastics: Global Lessons and Research to Inspire Action and Guide Policy Change *UNEP - UN Environ. Programme*. Available at <http://www.unep.org/resources/publication/marine-plastic-debris-and-microplastics-global-lessons-and-research-inspire> (Accessed 12 July 2021).
- Goudie, A. S., and N. J. Middleton 2006. Desert dust in the global system. *SSBM*
- Graham, W. F. and A. D. Duce 1979. Atmospheric pathways of the phosphorus cycle. *Geochim. Cosmochim. Acta* 43 (8):1195-1208. doi: 10.1016/0016-7037(79)90112-1.
- Griffin, D.W., C.A. Kellogg, and E.A. Shinn 2001. Dust in the Wind: Long Range Transport of Dust in the Atmosphere and Its Implications for Global Public and Ecosystem Health. *Glob. Chang. Hum. Health* 2, 20–33 doi:10.1023/A:1011910224374
- Ibrahim, A.H., P.F. Dunn, and R.M. Brach 2004. Microparticle detachment from surfaces exposed to turbulent air flow: Effects of flow and particle deposition characteristics. *J. Aerosol Sci.* 35 (7):805–821. doi:10.1016/j.jaerosci.2004.01.002.
- Jurcik, B. and H.-C. Wang 1991. The modelling of particle resuspension in turbulent flow. *J. Aerosol Sci., Proceedings of the 1991 European Aerosol Conference* 22:S149–S152. doi:10.1016/S0021-8502(05)80056-4.
- Katija, K., C.A. Choy, R.E. Sherlock, A.D. Sherman, and B.H. Robison 2017. From the surface to the seafloor: How giant larvaceans transport microplastics into the deep sea. *Sci. Adv.* 3 (8):e1700715. doi:10.1126/sciadv.1700715.
- Kim, Y., G. Wellum, K. Mello, K.E. Strawhecker, R. Thoms, A. Giaya, and B.E. Wyslouzil 2016. Effects of relative humidity and particle and surface properties on particle resuspension rates. *Aerosol Sci. Technol.* 50 (4):339–352. doi:10.1080/02786826.2016.1152350.
- Klein, M. and E. K. Fischer 2019. Microplastic abundance in atmospheric deposition within the Metropolitan area of Hamburg, Germany. *Sci. Tot. Envir.* 685:96-103. doi: 10.1016/j.scitotenv.2019.05.405.
- Krauter, P. and A. Biermann 2007. Reaerosolization of Fluidized Spores in Ventilation Systems. *Appl Environ. Microbiol* 73 (7):2165–2172. doi:10.1128/AEM.02289-06.
- Levermore, J. M., T. E. L. Smith, F. J. Kelly, and S. L. Wright 2020. Detection of Microplastics in Ambient Particulate Matter Using Raman Spectral Imaging and Chemometric Analysis. *Anal. Chem.* 92 (13), 8732-8740 DOI: 10.1021/acs.analchem.9b05445
- Loosmore, G.A. 2003. Evaluation and development of models for resuspension of aerosols at short times after deposition. *Atmos. Environ.* 37 (5):639–647. doi:10.1016/S1352-2310(02)00902-0.
- Mbachu, O., G. Jenkins, C. Pratt, and P. Kaparaju 2020. A New Contaminant Superhighway? A Review of Sources, Measurement Techniques and Fate of Atmospheric Microplastics. *Water Air Soil Pollut* 231 (2):85. doi:10.1007/s11270-020-4459-4.
- Morman S.A. and G.S. Plumlee 2014. Dust and Human Health. In: Knippertz P., Stuut JB. (eds) *Mineral Dust*. Springer, Dordrecht. https://doi.org/10.1007/978-94-017-8978-3_15
- Moulin, C., C. Lambert, F. Dulac, and U. Dayan 1997. Control of atmospheric export of dust from North Africa by the North Atlantic Oscillation. *Nature* 387, 691–694. doi:10.1038/42679

- Nicholson, K.W. 1988. A review of particle resuspension. *Atmos. Environ.* 22 (12):2639-2651 doi: 10.1016/0004-6981(88)90433-7
- Nicholson, K.W. 1993. Wind tunnel experiments on the resuspension of particulate material. *Atmos. Environ.* 27 (2):181–188. doi:10.1016/0960-1686(93)90349-4.
- Orgill, M. M., G. A. Sehmel, and M. R. Petersen 1976. Some Initial Measurements of Airborne DDT over Pacific North-west Forests. *Atmos. Environ.*, 10 (10)s:827–834. doi: 10.1016/0004-6981(76)90137-2
- Prata, J. C., J. L. Castro, J. P. da Costa, A. C. Duarte, T. Rocha-Santos, and M. Cerqueira 2020 The importance of contamination control in airborne fibers and microplastic sampling: Experiences from indoor and outdoor air sampling in Aveiro, Portugal. *Mar. Pollut. Bull.* 159 doi: 10.1016/j.marpolbul.2020.111522.
- Rahman, L., G. Mallach, R. Kulka, and S. Halappanavar 2022 Microplastics and nanoplastics science: collecting and characterizing airborne microplastics in fine particulate matter. *Nanotoxicology*, DOI: 10.1080/17435390.2021.2018065
- Reeks, M.W. and D. Hall 2001. Kinetic models for particle resuspension in turbulent flows: theory and measurement. *J. Aerosol Sci.* 32 (1):1–31. doi:10.1016/S0021-8502(00)00063-X.
- Rezaei, M., M.J.P.M. Riksen, E. Sirjani, A. Sameni, and V. Geissen 2019. Wind erosion as a driver for transport of light density microplastics. *Sci. Total Environ.* 669:273–281. doi:10.1016/j.scitotenv.2019.02.382.
- Ritchie, H. and M. Roser 2018. Plastic Pollution. *Our World Data*.
- SAPEA (2019). A Scientific Perspective on Microplastics in Nature and Society. SAPEA, DE.
- Savoie, D. L. and J. M. Prospero 1980. Water-Soluble Potassium, calcium, and magnesium in the aerosols over the Tropical North Atlantic. *J. Geophys. Res.*, 85 (C1): 385–392, doi:10.1029/JC085iC01p00385.
- Soltani, M. and G. Ahmadi 1994. On particle adhesion and removal mechanisms in turbulent flows. *J. Adhes. Sci. Technol.* 8 (7):763–785. doi:10.1163/156856194X00799.
- Stefánsson, H., M. Peternell, M. Konrad-Schmolke, H. Hannesdóttir, E.J. Ásbjörnsson, and E. Sturkell 2021. Microplastics in Glaciers: First Results from the Vatnajökull Ice Cap. *Sustainability* 13 (8):4183. doi:10.3390/su13084183.
- Thomas, C.K., B.E. Law, J. Irvine, J.G. Martin, J.C. Pettijohn, and K.J. Davis 2009. Seasonal hydrology explains interannual and seasonal variation in carbon and water exchange in a semiarid mature ponderosa pine forest in central Oregon. *J. Geophys. Res. Biogeosciences* 114 (G4). doi:https://doi.org/10.1029/2009JG001010.
- Vianello, A., R.L. Jensen, L. Liu, and J. Vollertsen 2019. Simulating human exposure to indoor airborne microplastics using a Breathing Thermal Manikin. *Sci Rep* 9, 8670 https://doi.org/10.1038/s41598-019-45054-w
- Wang HC. 1991 Reducing Uncertainties in Particle Adhesion and Removal Measurements. In: Mittal K.L. (eds) *Particles on Surfaces* 3. Springer, Boston, MA. https://doi.org/10.1007/978-1-4899-2367-7_15
- Weis, C. P., A. J. Intrepido, A. K. Miller, P. G. Cowin, M. A. Durno, J. S. Gebhardt, and R. Bull 2002. Secondary aerosolization of viable *Bacillus anthracis* spores in a contaminated US Senate Office. *JAMA*, 288(22), 2853–2858. https://doi.org/10.1001/jama.288.22.2853
- Wen, H.Y. and G. Kasper 1989. On the kinetics of particle reentrainment from surfaces. *J. Aerosol Sci.* 20 (4):483–498. doi:10.1016/0021-8502(89)90082-7.
- Wu, Y.-L., C.I. Davidson, and A.G. Russell 1992. Controlled Wind Tunnel Experiments for Particle Bounceoff and Resuspension. *Aerosol Sci. Technol.* 17 (4):245–262. doi:10.1080/02786829208959574.
- Zhang, Y., S. Kang, S. Allen, D. Allen, T. Gao, and M. Sillanpää 2020. Atmospheric microplastics: A review on current status and perspectives. *Earth Sci. Rev.*, 203, 103118. doi: 10.1016/j.earscirev.2020.103118
- Zimon, A.D. 1982. *Adhesion of Dust and Powder*. Springer US, Boston, MA.

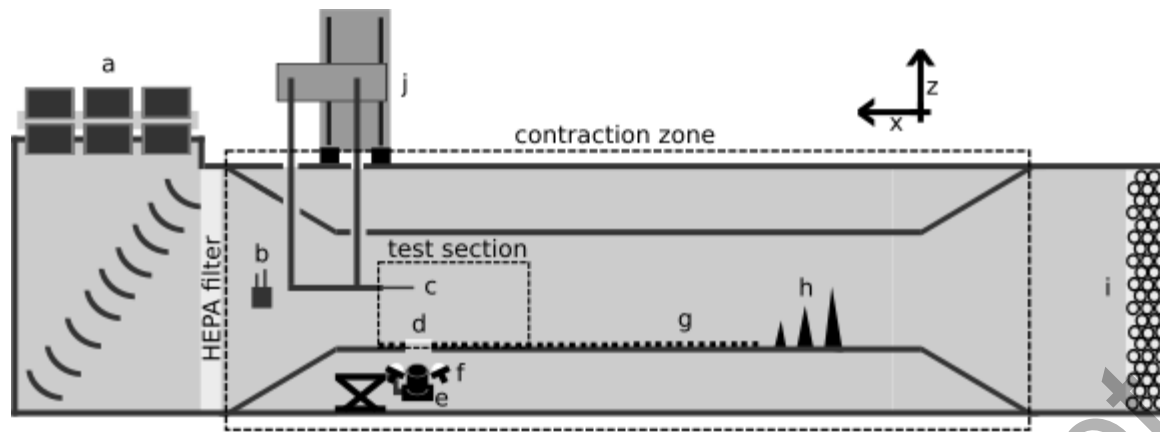


Figure 1. A simplified illustration of the wind tunnel setup. a) fans; b) temperature and humidity sensors; c) constant temperature anemometer; d) glass plate; e) visual camera with lift; f) ultra-violet lights; g) roughness elements; h) cones; i) honeycomb structure; j) 1D-traverse

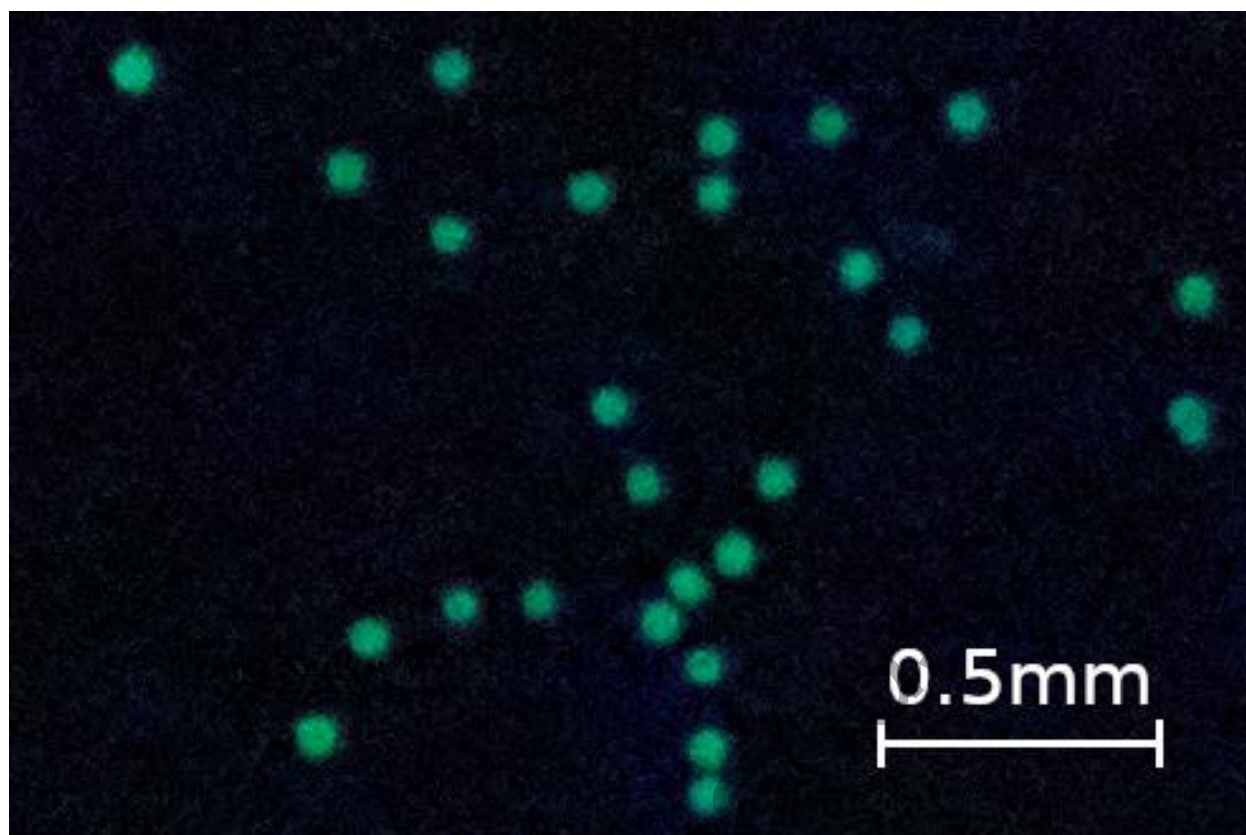


Figure 2. Cutout of an original image showing 26 fluorescent microplastic particles (fMPPs). This image was used for the color intensity threshold evaluation of fMPP type A.

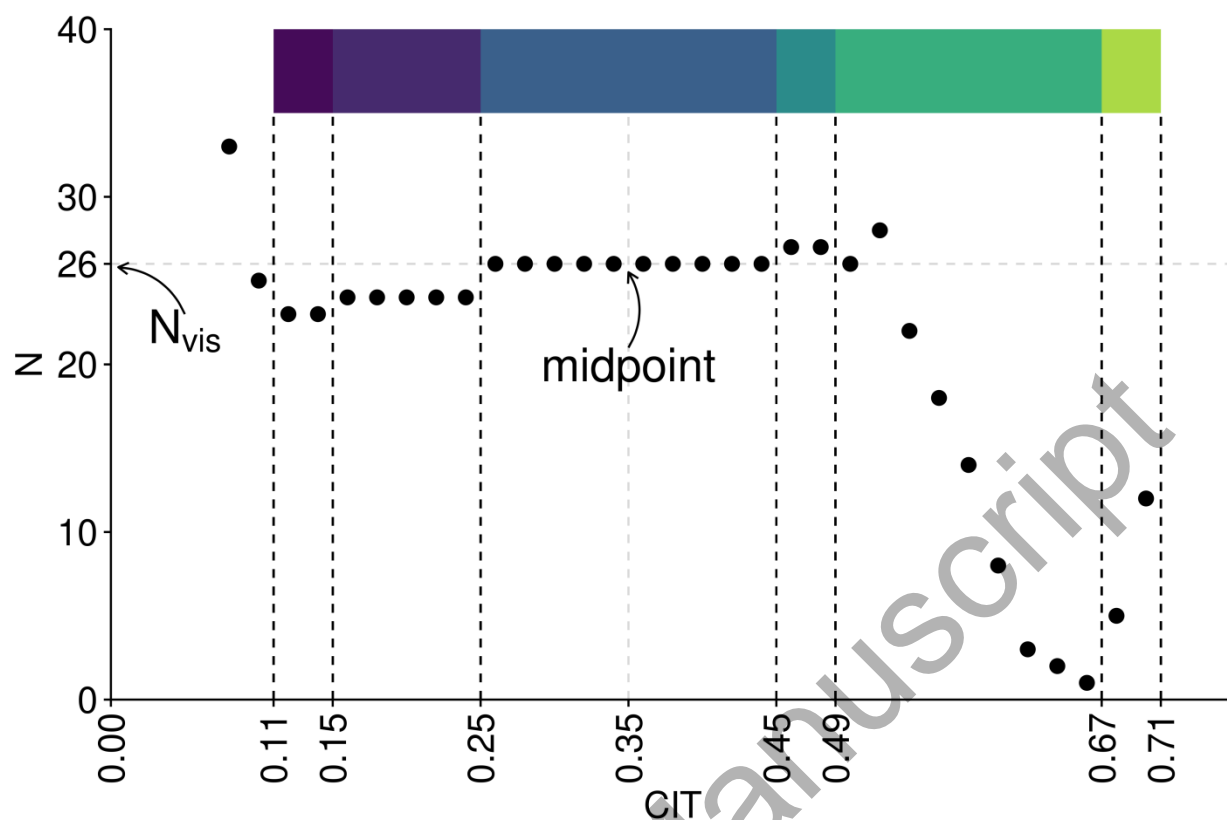


Figure 3. Dependence of number of microplastic particles detected (N) versus the user-selected color intensity threshold (CIT) across the range of 0.02 to 0.7 for fMPP type A. The horizontal dashed gray line indicates the visually determined N (N_{vis}). The vertical dashed gray line indicates the midpoint of the CIT range that determined N equal to N_{vis} . The color bar on top of the segments enclosed by dashed lines correspond to the colored pixels in figure 4. Not shown are the data points CIT = 0.02, 0.04, 0.06 and their respective estimate for $N = 566, 748, 146$.

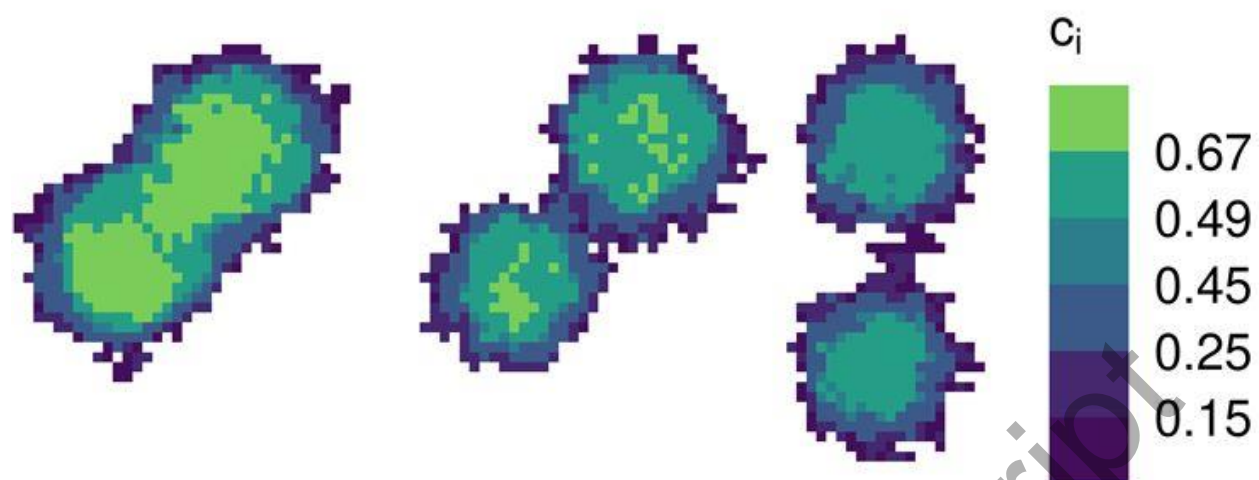


Figure 4. Color intensity (c_i) of pixels in three different clusters comprising two particles. The binned color gradient corresponds to the color bar in figure 3.

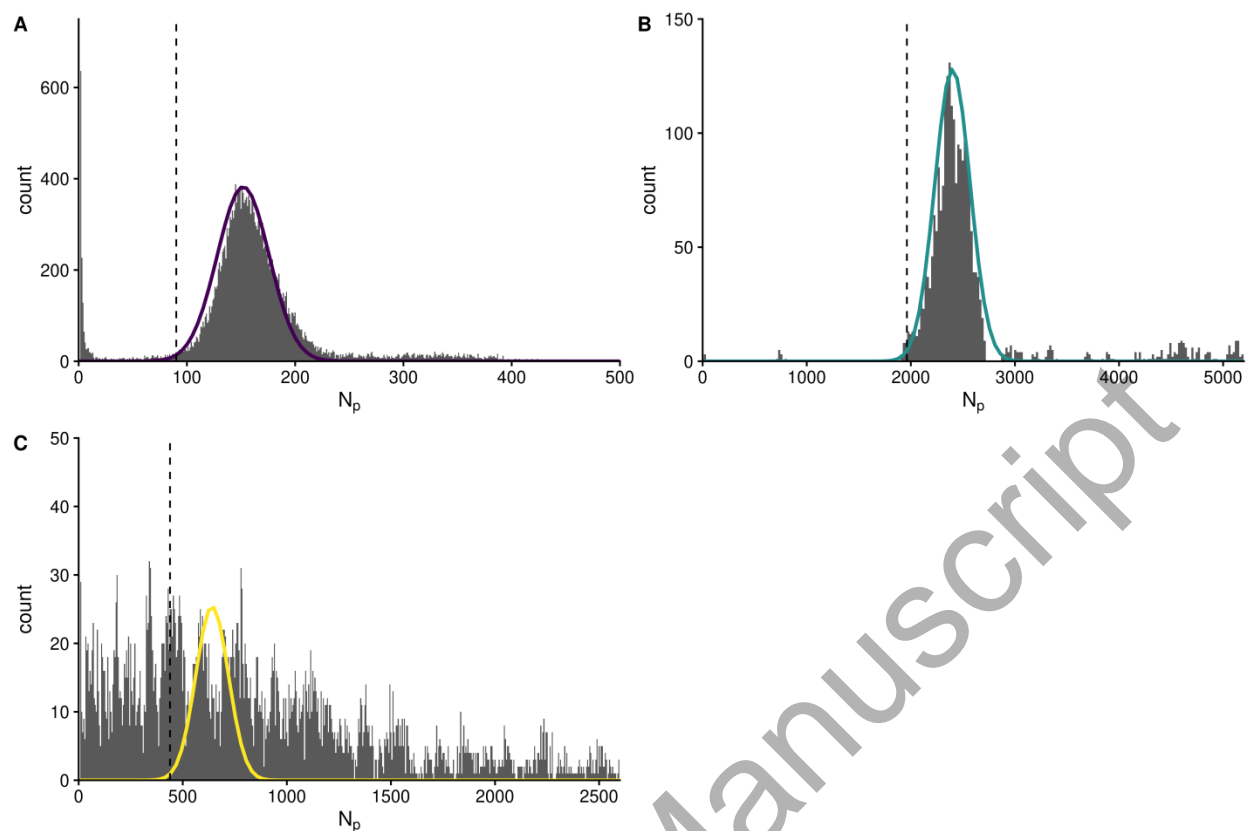


Figure 5. Histogram of the number of pixels a particle contains (N_p) for fMPP type A in A), fMPP type B in B) and fMPP type C in C). The solid line represents a normal distribution that was fit to the main peak found for the distribution of N_p . The dashed line represents the minimal N_p value that was used for the further analysis (N_f). The distribution parameters for fMPP type C were derived from original size distribution provided in the data sheet (see Fig. S10).

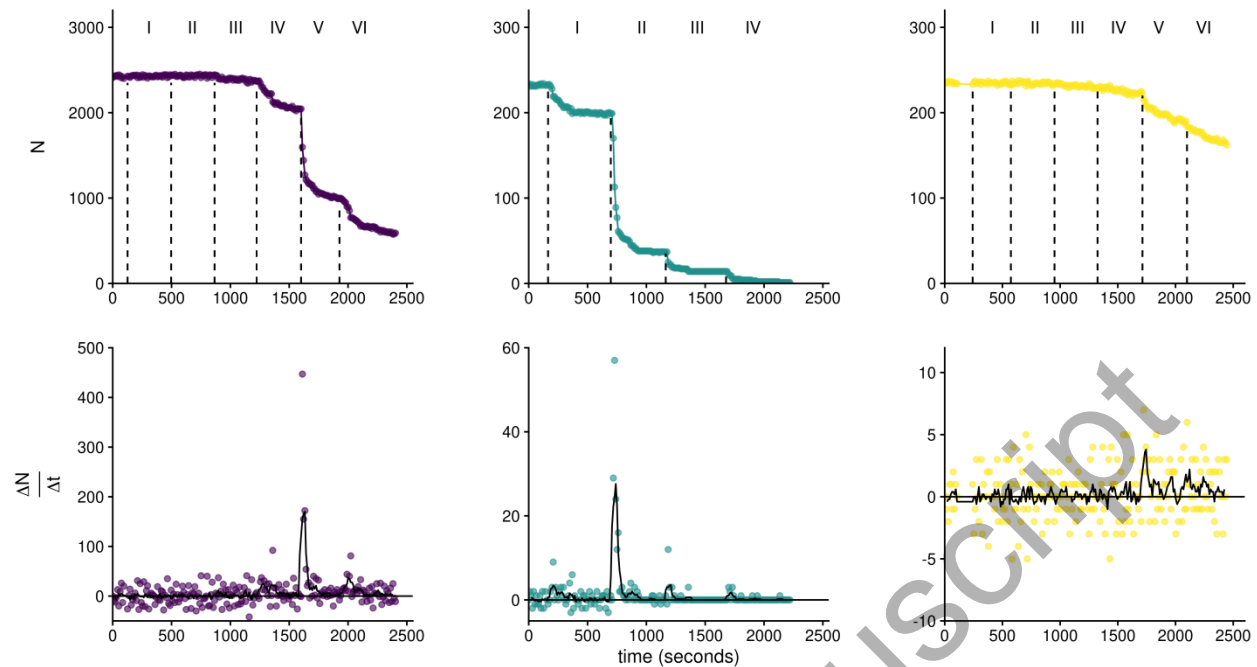


Figure 6. The total number of particles remaining on the glass plate (N) and the suspension rate ($\frac{\Delta N}{\Delta t}$) with respect to time for the three fMPP types. Column A shows the results of fMPP type A, column B of fMPP type B and column C of fMPP type C. The blackline fitted to $\frac{\Delta N}{\Delta t}$ represents a 50 second rolling-mean. The roman numbers indicate the individual suspension stages. The value of $u_{*,EC}$ was raised from suspension stage one to six. The data before suspension stage one are part of suspension stage zero. Values for $u_{*,EC}$ employed in the suspension stages can be found in Table 1.

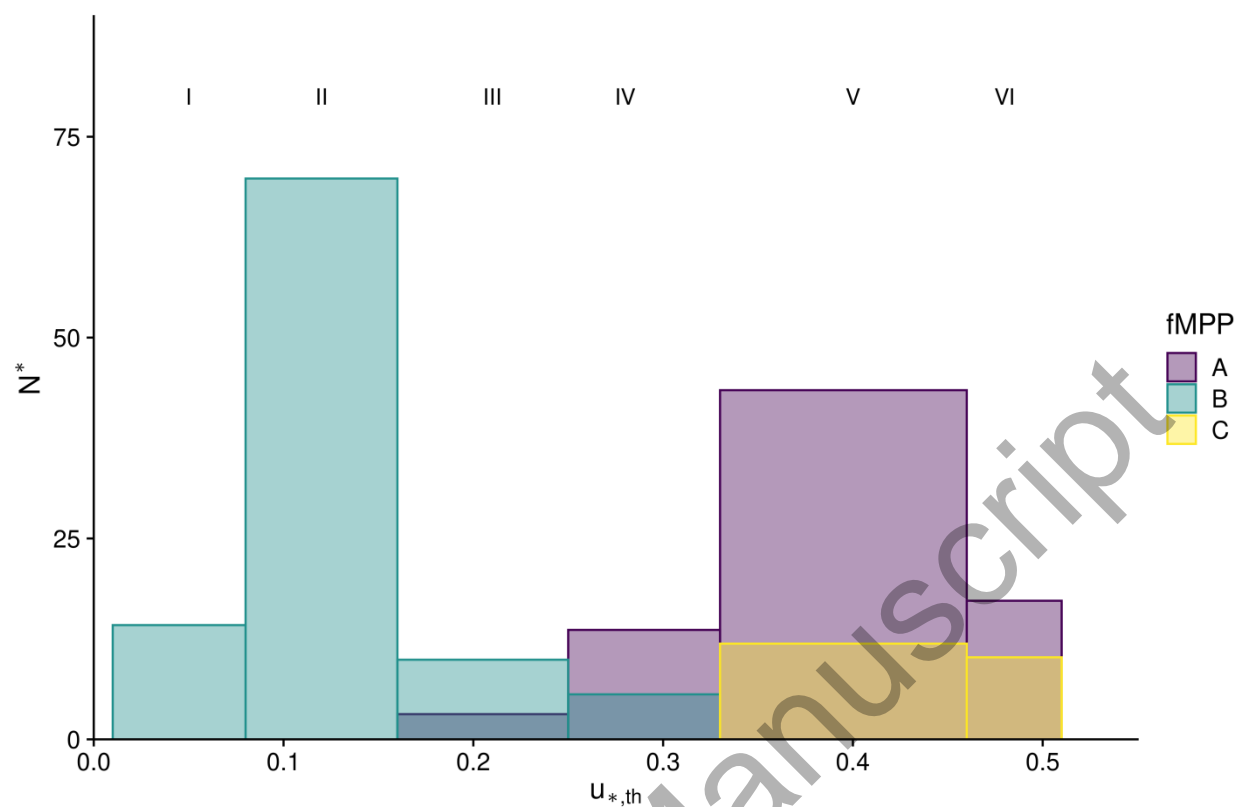


Figure 7. The fraction of suspended fMPPs (N^*) with respect to the friction velocity for all three fMPP types. The roman numbers indicate the individual suspension stages. The right border of a bar corresponds to the threshold friction velocity ($u_{*,th}$) of the suspension stage.

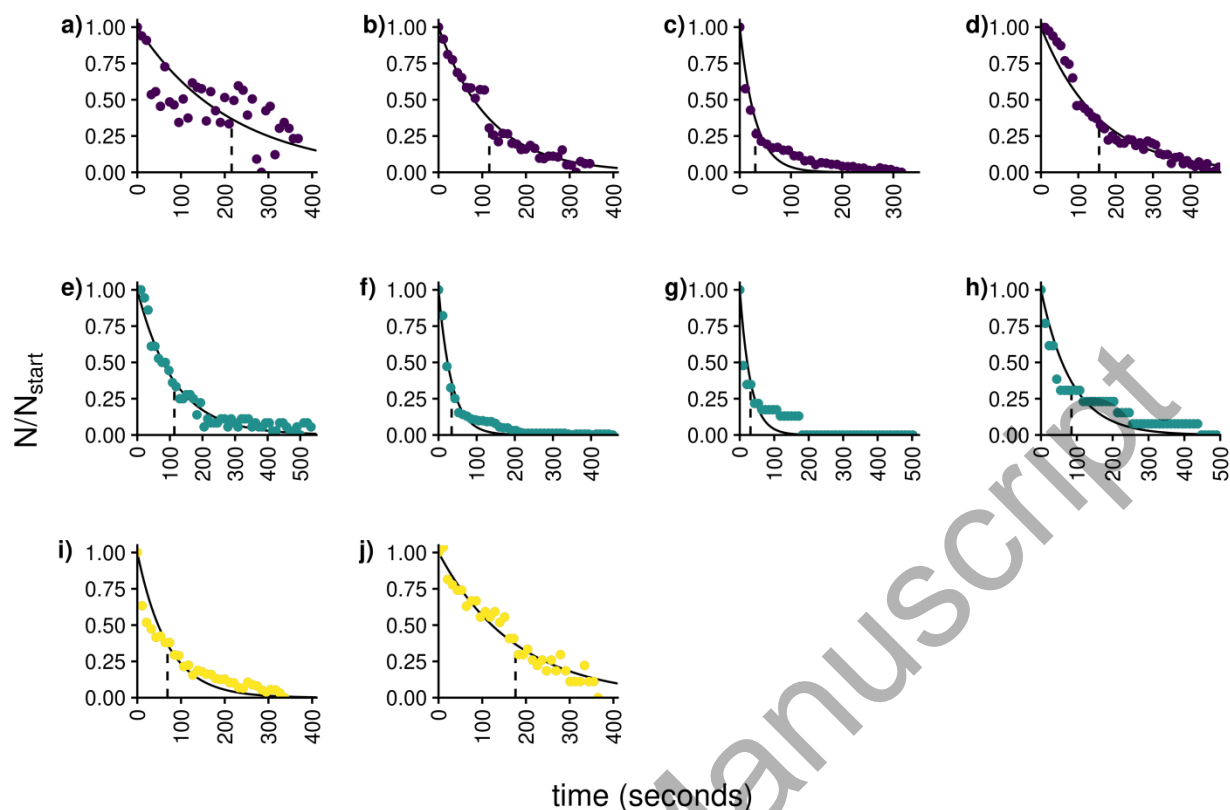


Figure 8. Normalized number of particles residing on the glass plate with respect to time. The number of particles was normalized by the number of particles at the start of the individual suspension stages. Black lines represent exponential decay functions fitted to the suspension stages (S). The dashed lines indicate the time constant (τ). a) = fMPP type A:S3; b)= fMPP type A:S4; c)= fMPP type A:S5; d)= fMPP type A:S6; e)= fMPP type B:S1; f)= fMPP type B:S2; g) = fMPP type B:S3; h)= fMPP type B:S4; i)= fMPP type C:S5; j)= fMPP type C:S6

Table 1 Results of the vibration experiment. N is the mean total amount of particles detected; \bar{N}_p is the mean number of pixels a particle contained; \bar{U}_{27mm} is the mean wind speed in ms^{-1} ; ISO is the camera's sensor sensitivity to light; Shutter speed in s; Aperture in the focal ratio. Here the mean of N and \bar{N}_p are presented with their relative standard deviation.

<u>Set</u>	<u>\bar{U}_{27mm}</u>	<u>Camera Setup</u>	<u>ISO</u>	<u>Shutter speed</u>	<u>Aperture</u>	<u>N</u>	<u>\bar{N}_p</u>
<u>1</u>	<u>0</u>	<u>A</u>	<u>2500</u>	<u>1/10</u>	<u>f/2.8</u>	<u>1661+0.1</u>	<u>195.8+0.4</u>
<u>2</u>	<u>5.2</u>	<u>A</u>	<u>2500</u>	<u>1/10</u>	<u>f/2.8</u>	<u>1623+1.1</u>	<u>229+8</u>
<u>3</u>	<u>5.2</u>	<u>B</u>	<u>51200</u>	<u>1/320</u>	<u>f/2.8</u>	<u>1644+0.2</u>	<u>171+3</u>

Table 2 Results and values used for the individual suspension stages (Sus.stage). \bar{U}_{27mm} wind speed in ms^{-1} at $z = 27 \text{ mm}$; u_* derived from the wind profile ($u_{*,PR}$) and directly measured ($u_{*,EC}$) in ms^{-1} ; N^* in %; time constant (τ) in s.

				fMPP	A	fMPP	B	fMPP	C
Sus.stage	\bar{U}_{27mm}	$u_{*,EC}$	$u_{*,PR}$	N^*	τ	N^*	τ	N^*	τ
0	0	0	0	0	NA	0	NA	0	NA
I	0.9+0.02	0.08	0.08	0	NA	14	113	0	NA
II	1.6+0.02	0.16	0.17	0	NA	70	33	0	NA
III	2.4+0.05	0.25	0.25	3	195	10	31	0	NA
IV	3.1+0.06	0.33	0.3	13	117	6	85	0	NA
V	4.2+0.05	0.46	0.4	43	30	0	NA	8	69
VI	5.2+0.05	0.51	0.47	17	152	0	NA	7	159